Supplementary Information

Highly Efficient Photocatalytic Water Splitting Utilizing $WO_{3-x}/ZnIn_2S_4$ Ultrathin Nanosheets Z-Scheme Catalyst

Dian Luo,[1] Lei Peng,[1] Yang Wang,[1] Xiangyu Lu,[1] Cheng Yang,[2] Xinsheng Xu,[2] Yucheng Huang,[1*] and Yonghong Ni[1*]

[1] College of Chemistry and Materials Science, Key Laboratory of Functional Molecular Solids, Ministry of Education, Anhui Laboratory of Molecule-Based Materials, Anhui Key Laboratory of Functional Molecular Solids, Anhui Normal University, 189 Jiuhua Southern Road, Wuhu, 241002, PR. China. Email: huangyc@mail.ahnu.edu.cn (Y.C. Huang); niyh@mail.ahnu.edu.cn (Y.H. Ni)

[2] School of Physics and Electronic Information, Anhui Normal University, 189 Jiuhua Southern Road, Wuhu, 241002, P.R. China.

Experimental section

Reagents. Citric acid (AR), glucose (AR), thioacetamide (CH_3CSNH_2, ⩾99%), triethanolamine (TEOA), and glycerine were purchased from Sinopharm Chemical Reagent Co., Ltd. Zinc chloride ($ZnCl_2$, 98%) and sodium tungstate dishydrate ($Na_2WO_4{\cdot}2H_2O$, 99.5%) were obtained from Macklin. Indium chloride tetrahydrate ($InCl_3{\cdot}4H_2O$, ⩾98%) was bought from Aladdin. The ultrapure water was used in all experiments. All chemicals were directly used without further purification.

Synthesis of WO_{3-x} nanosheets. The defective tungsten trioxide nanosheets were synthesized according to a reported method with some modifications.[1] In a typical synthesis, 1 mmol of $Na_2WO_4 \cdot 2H_2O$ was added into 30 mL of H_2O to form a transparent solution; and subsequently, 1.5 mmol of citric acid and 5 mmol of glucose were introduced in order. After stirring for 10 min, 3 mL 6 M of HCl was added into the above solution with continuously stirring for another 30 min. The mixed solution was then transferred into a 50 mL Teflon-lined autoclave and heated at 120 °C for 24 h. After the autoclave had cooled down to room temperature naturally, the product was collected by centrifugation, washed with water and anhydrous ethanol several times, dried at 333 K in vacuum oven for 24 h. Finally, the obtained powder was calcined in Ar gas at a heating rate of 2 °C/min and maintained at 400 °C for two hours. After cooling to room temperature naturally, the dark-blue powder was obtained for further use and characterization.

Synthesis of $WO_{3-x}/ZnIn_2S_4$ ultrathin nanosheets heterojunction. To construct $WO_{3-x}/ZnIn_2S_4$ ultrathin nanosheets heterojunction, a mild oil bath heating route was designed. Briefly, 10 mg WO_{3-x} powder was firstly dispersed in a solvent consisted of 8 mL H_2O and 2 mL glycerine under stirring. After continuously stirring for 20 min, 27.7 mg $ZnCl_2$, 59.7 mg $InCl_3 \cdot 4H_2O$, and 30 mg thioacetamide were introduced. After stirring for another 5 min, the mixed solution was transferred into a flask and kept at 80 °C for 2 h. The final product was collected by centrifugation and washed with water and anhydrous ethanol three times, and dried at 60 °C in vacuum overnight.

Synthesis of pristine $ZnIn_2S_4$ nanoflowers composed of nanosheets. 27.7 mg $ZnCl_2$, 59.7 mg $InCl_3 \cdot 4H_2O$, and 30 mg thioacetamide were introduced to a solvent consisted of 8 mL H_2O and 2 mL glycerine under stirring, then the mixed solution was transferred into a flask and kept at 80 °C

for 2 h. The final product was collected by centrifugation and washed with water and anhydrous ethanol three times, and dried at 60 °C in vacuum overnight.

Characterization. The crystal phases and chemical compositions of the samples were analyzed by X-ray diffraction (XRD) on a Bruker D8 X-Ray Diffractometer with Cu $K\alpha$ radiation (λ = 1.5406 Å). Transmission electron microscopy (TEM) images of the products were taken on a Hitachi HT7700 transmission electron microscope at an acceleration voltage of 120 kV. The valence state of the element and the valence band spectra were detected by X-ray photoelectron spectroscopy, which were carried out on an ESCALAB 250Xi instrument with a monochromatic Al Kα (hν = 1486.6 eV), the X-ray beam spot was 500 μm with the transmittance of 30 eV. The lattice fringe and selected area electron diffraction (SAED) were obtained by high resolution transmission (HRTEM) in Tecnai G2 (Thermo Fisher Scientific). The morphology and element mapping were conducted with aberration-corrected high-angle annular dark-field scanning transmission electron microscopy (HAADF-STEM) on FEI Talos F200X (Thermo Fisher Scientific). Room-temperature UV–vis diffuse reflectance spectroscopy was performed on a UV–vis–NIR spectrophotometer (Perkin Elmer Lambda 950). ESR spectra were collected at room temperature using a JEOL JES-X310 electron spin resonance spectrometer (298 K, 9.062 GHz). Steady state fluorescence spectra were conducted at FLSP 920 (Edinburgh Instruments, UK). Decay curves of the time-resolved fluorescence spectra were obtained on a FLS1000 fluorescence lifetime spectrophotometer (Edinburgh Instruments). All electrochemical measurements were performed on a CHI660E electrochemical station (Chenhua, Shanghai). Electrochemical impedance spectroscopy (EIS) was conducted at the open circuit potential over the frequency range from 10^{-2} to 10^{5} Hz with AC signals of amplitude of 5 mV. The fitting results of EIS were

obtained by using Zsimpwin software. The measurements were carried out in a three-electrode system with the graphite rod as the counter electrode and an Ag/AgCl as the reference electrode at room temperature in 0.5 M Na_2SO_4 solution. The working electrodes were prepared as follows: 2 mg of catalysts were firstly dispersed into a mixed solvent of 2 mL ethanol and 10 μL Nafion under the ultrasound assistance; and then, the formed slurry was coated on Ni foam with the size of 1 × 1 cm^2. The LSV curves were run at a rate of 1 $mV \cdot s^{-1}$ with 85% iR compensation. The photocurrent measurements were performed with the irradiation of the periodic light under the same conditions as the electrochemical impedance experiments, employing the indiumtin oxide (ITO) glass (1 × 1 cm^2) coated with the photocatalyst slurry as the photoelectrodes.

Photocatalytic hydrogen production measurements. Typically, 5 mg of the photocatalyst, 2 mL of triethanolamine (TEOA), and 10 mL of H_2O were added into a gas-closed glass vacuum system with 100 mL in capacity. A 300W Xe lamp with a 400 nm cutoff filter and full solar spectral band reflector was used as the light source. During the photocatalytic process, the reaction system was vigorously stirred with a magnetic stirrer, and the reaction temperature was controlled at 6 °C by circulating cooling water. After each reaction, the generated H_2 was sampled and quantified by gas chromatography with Ar as the carrier gas.

Ultrafast transient absorption (TA) spectroscopy characterizations. The femtosecond transient absorption measurements were performed based on a 1 kHz Ti:Sapphire Coherent Astrella regenerative amplifier from Coherent (6 mJ/pulse, 35 fs (fwhm) at 800 nm) combined with Helios transient absorption spectrometer (Ultrafast Systems). Briefly, the fundamental output beam was split into two parts with a 50% beam splitter. The transmitted part was directed into a TOPAS Optical Parametric Amplifier (OPA) to generate tunable excitation (250 nm ~ 2.5 μm) as

pump beam. The other part with less than 10% was used to generate a white light continuum which was used for probe beam. The pump and probed beam were focused and overlapped into a spot on the solution. Solution was transferred into a 2-mm pathlength quartz cuvette and was stirred continuously throughout the whole experiment. All transient spectra and kinetics were obtained by averaging at least five scans and performed at room temperature.

Calculation details. Density functional theory (DFT) calculations were implemented using the Vienna ab initio Simulation Package (VASP) with the projector-augmented wave pseudopotentials.[2] The generalized gradient approximation in the form of Perdew−Burke−Ernzerhof (PBE) was adopted.[3] An energy cutoff of 500 eV was used for the plane-wave basis set. The residual energy and force convergence criterion was 10^{-5} eV and 0.02 eV $Å^{-1}$, respectively. A vacuum space of at least 15 Å was applied to avoid interactions between two periodic units. The Brillouin zone was represented by 5×5×1 Gamma-centered mesh of k-points for geometry optimizations, whereas a larger grid of 9×9×1 was used for electronic properties computations. In order to avoid the underestimate of the bandgap calculated within PBE, the hybrid functional of Heyd–Scuseria–Ernzerhof (HSE06) [4] was used to obtain more accurate electronic band structures.

To calculate hydrogen adsorption Gibbs free energy (ΔG_{H*}), an interfacial model was constructed. We first constructed a orthorhombic structure for (001) plane of $ZnIn_2S_4$, then built a 2×3×1 supercell, and finally put a defective 1×1×1 WO_{3-x} on it. The lattice mismatch along x direction for the $ZnIn_2S_4/WO_{3-x}$ model is within 6%. Due to the slight influence on the ΔG_{H*}, the solvation effect is not taken into account in this work.[5]

According to the methodology developed by Nørskov et al.,[6] the chemical potential of $H^+ + e^-$ is

equal to that of 1/2 H_2 at standard condition (pH = 0, P_{H2} = 1 bar, T = 298 K). ΔG_{H*} was considered to characterize the hydrogen evolution reaction (HER) activity:

$$\Delta G_{H*} = \Delta E_{H*} + \Delta E_{ZPE} - T\Delta S$$

Where ΔE_{H*} is the difference of hydrogen adsorption energy, which can be calculated using the formula of $\Delta E_{H*} = E_{T+H*} - E_T - 1/2\ E_{H2}$. Here E_{T+H*}, E_T and $1/2\ E_{H2}$ represent the total energies of $ZnIn_2S_4/WO_{3-x}$ heterostructure with one hydrogen atom adsorbed on the interface, $ZnIn_2S_4/WO_{3-x}$ heterostructure and H_2 molecule, respectively. ΔE_{ZPE} is the difference in zero-point energy between the adsorbed H* and molecular H_2 in gas phase, which can be obtained via vibrational frequency calculations; T is the temperature (set as 298.15 K), and ΔS is the difference in entropy.

Experimental evidence for Z-scheme charge transfer mechanism. According to the method described by Li et al.,[7] the photo-induced deposition was conducted to prove Z-scheme charge transfer mechanism indirectly. The photo-oxidation deposition of the MnO_x on WO_{3-x} nanosheets was achieved with $Mn(NO_3)_2$ as the Mn source, and the photo-reduction deposition of the Pt particles on $ZnIn_2S_4$ nanosheets was achieved with H_2PtCl_6 as the Pt source. Photocurrent measurements were conducted to elucidate the separation of photogenerated charges. As seen from the photocurrent response curves shown in Fig.S11, different from $WO_{3-x}/ZnIn_2S_4$, the photo-generated electrons migrated to the Pt particles on $ZnIn_2S_4$ nanosheets in $WO_{3-x}/ZnIn_2S_4/Pt$, and the photo-generated holes to MnO_x on WO_{3-x} nanosheets in $MnO_x/WO_{3-x}/ZnIn_2S_4$, respectively, which enhanced the photocurrent responses. The biggest photocurrent response was found in $MnO_x/WO_{3-x}/ZnIn_2S_4/Pt$. Thus, the Z-scheme charge transfer mechanism was proven indirectly.

References:

1 N. Zhang, X.Y. Li, H.C. Ye, S.M. Chen, H.X. Ju, D.B. Liu, Y. Lin, W. Ye, C.M. Wang, Q. Xu, J.F. Zhu, L. Song, J. Jiang, Y.J. Xiong, *J. Am. Chem. Soc.* 2016, ***138*,** 8928-8935.

2 a) G. Kresse, J. Furthmüller, *Phys. Rev. B* 1996, ***54***, 11169-11186; b) P. E. Blöchl, *Phys. Rev. B* 1994, ***50***, 17953-17979.

3 J.P. Perdew, K. Burke, M. Ernzerhof, Phys. Rev. Lett. 1996, ***77***, 3865-3868.

4 J. Heyd, G. E. Scuseria, *J. Chem. Phys.* 2004, ***121***, 1187-1192.

5 K. Mathew, R. Sundararaman, K. Letchworth-Weaver, T. A. Arias, R. G. Hennig, *J. Chem. Phys.* 2014, ***140***, 084106.

6 a) J. K. Norskov, J. Rossmeisl, A. Logadottir, L. Lindqvist, J.R. Kitchin, T. Bligaard, H. Jonsson, *J. Phys. Chem. B* 2004, ***108***, 17886-17892; b) B. Hinnemann, P.G. Moses, J. Bonde, K.P. Jorgensen, J.H. Nielsen, S. Horch, I. Chorkendorff, J.K. Norskov, *J. Am. Chem. Soc.* 2005, ***127***, 5308-5309; c) A. Valdes, Z.W. Qu, G.J. Kroes, J. Rossmeisl, J.K. Norskov, *J. Phys. Chem. C* 2008, ***112***, 9872-9879.

7 R.G. Li, F.X. Zhang, D.E. Wang, J.X. Yang, M.R. Li, J. Zhu, X. Zhou, H.X. Han, C. Li, Nat. Commun. 2013, **4**, 1432.

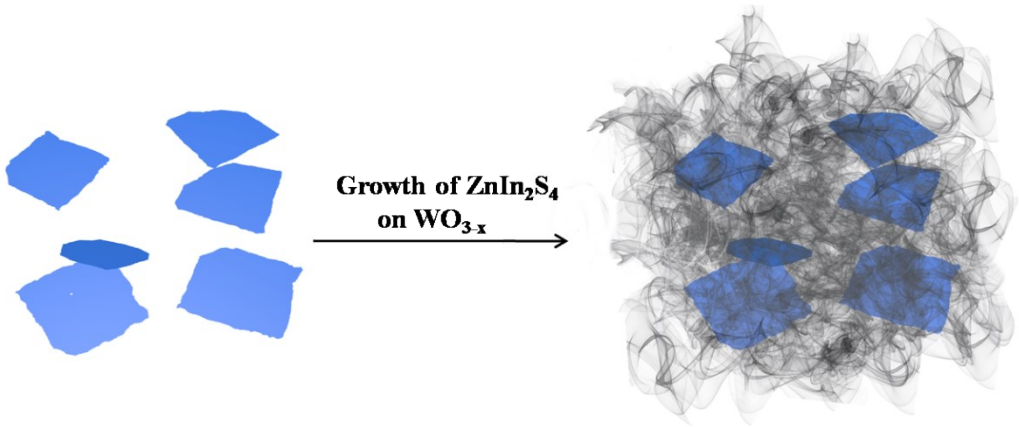

Supplementary Fig.1 Scheme for the synthesis of the $WO_{3-x}/ZnIn_2S_4$ ultrathin heterojunctions.

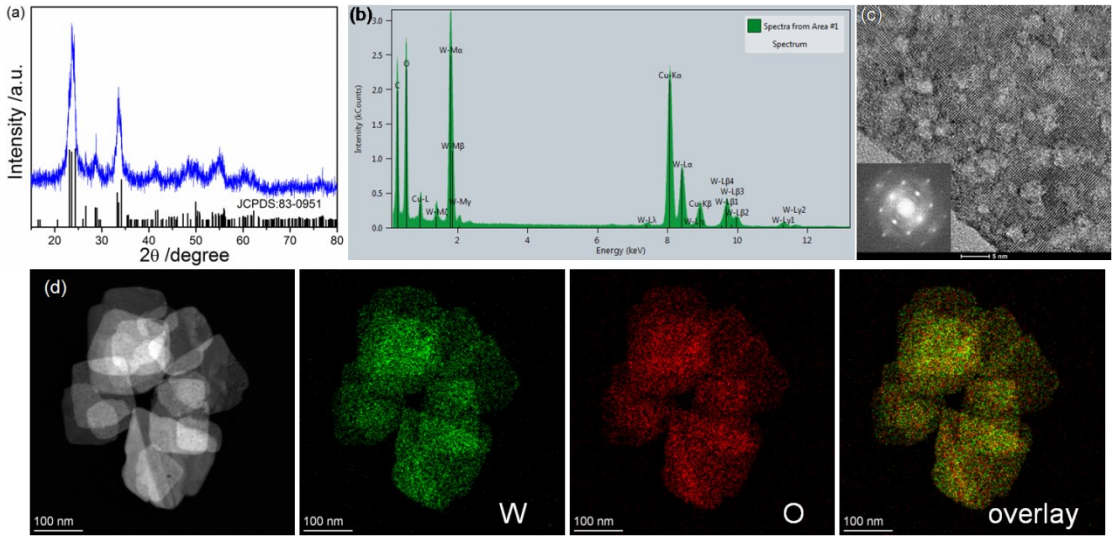

Supplementary Fig.2 (a) XRD pattern, (b) EDS analysis, (c) HRTEM and SAED pattern, (d) STEM and HAADF-STEM element mapping images of as-prepared WO_{3-x} nanosheets.

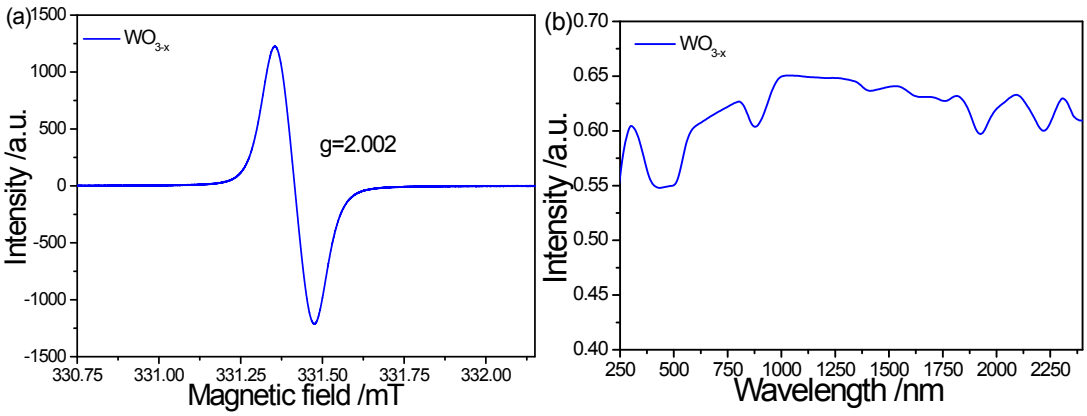

Supplementary Fig.3 (a) ESR and (b) UV-Vis-NIR diffuse reflectance spectra of as-prepared WO_{3-x} nanosheets.

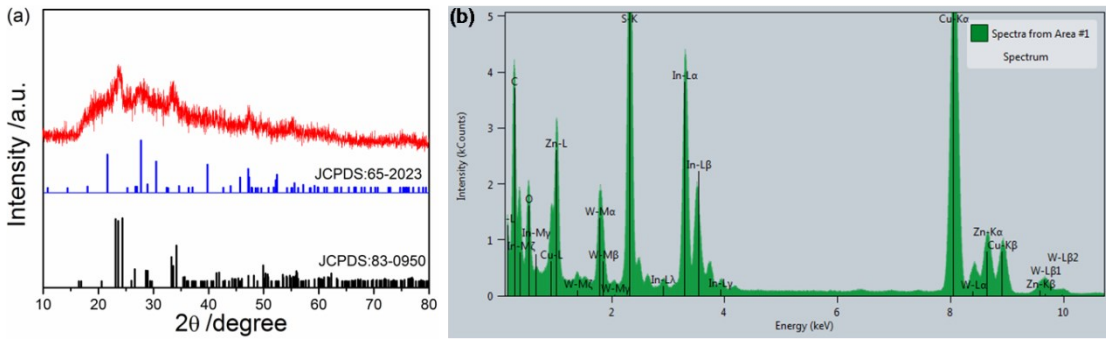

Supplementary Fig.4 (a) XRD pattern and (b) EDS analysis of as-prepared $WO_{3-x}/ZnIn_2S_4$ nanosheets heterostructures.

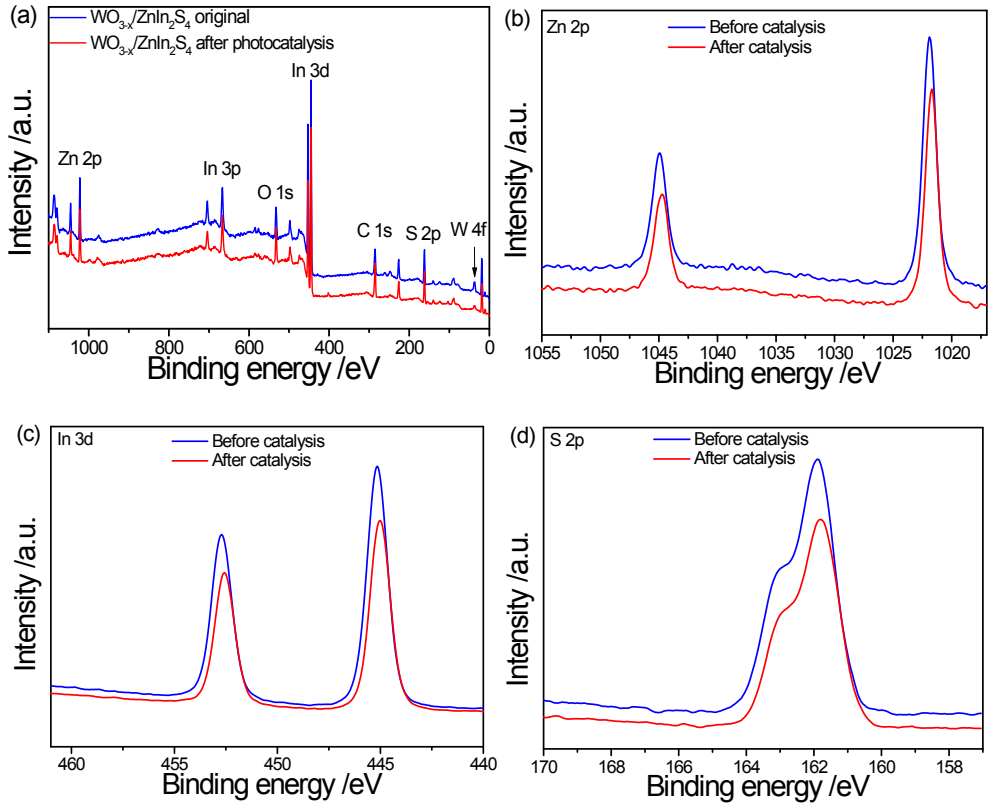

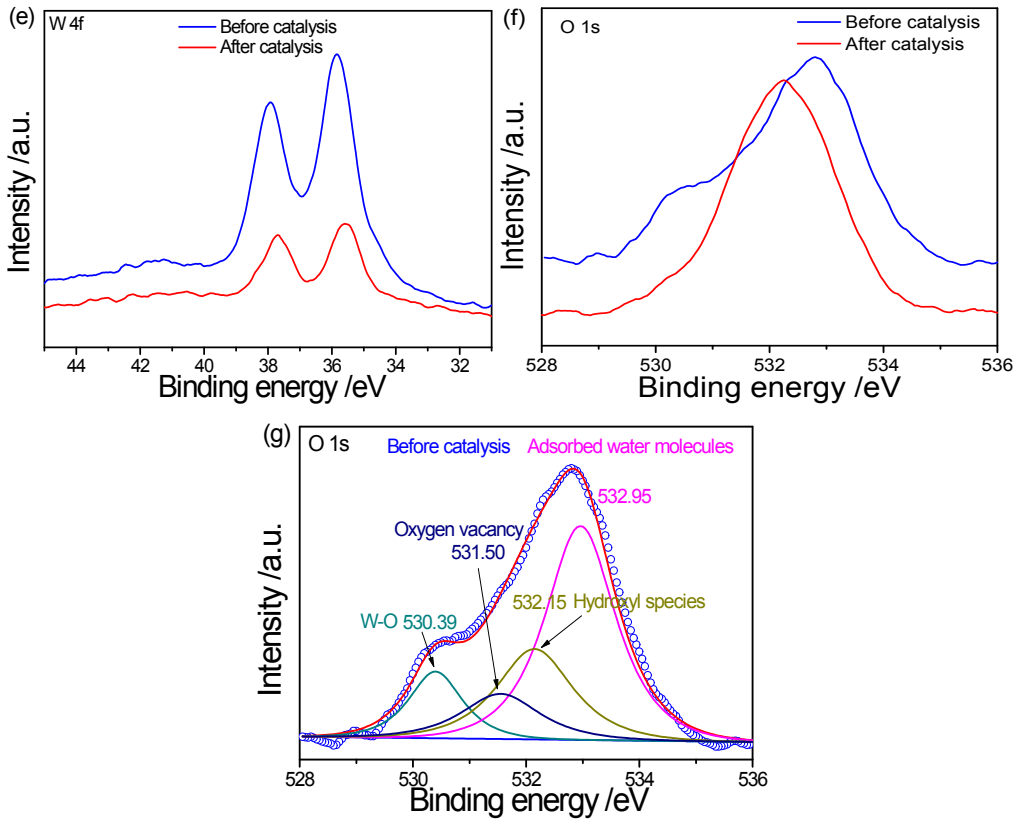

Supplementary Fig.5 (a) Survey spectra comparison of $WO_{3-x}/ZnIn_2S_4$ catalyst before and after photocatalysis. High resolution XPS spectra: (b) Zn 2p, (c) In 3d, (d) S 2p, (e) W 4f and (f and g) O 1s.

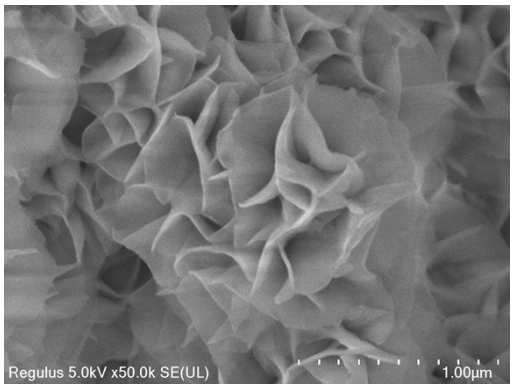

Supplementary Fig.6 Typical FESEM image of pristine $ZnIn_2S_4$ prepared under the same experimental conditions without the presence of WO_{3-x}.

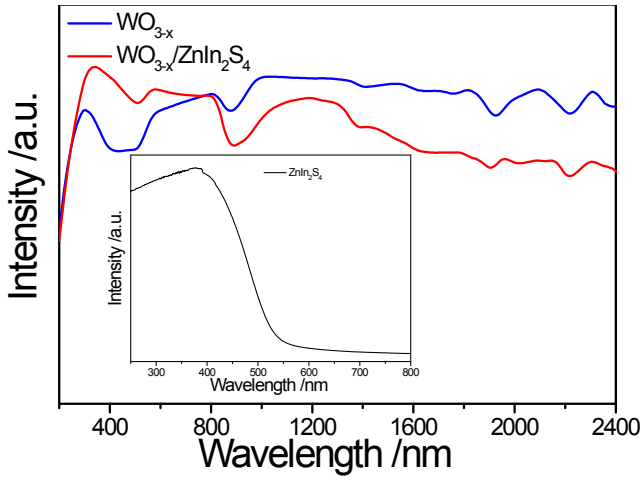

Supplementary Fig.7 UV-vis-NIR diffuse reflectance spectra of $ZnIn_2S_4$ (the inset), WO_{3-x} and $WO_{3-x}/ZnIn_2S_4$.

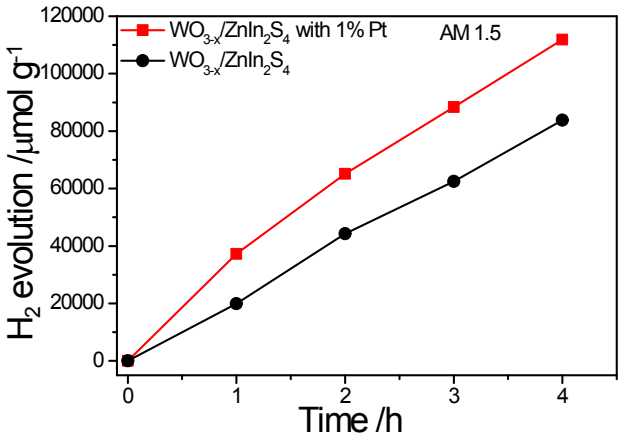

Supplementary Fig.8 The photocatalytic hydrogen evolution curves of $WO_{3-x}/ZnIn_2S_4$ without and with 1% of Pt under irradiation of AM 1.5.

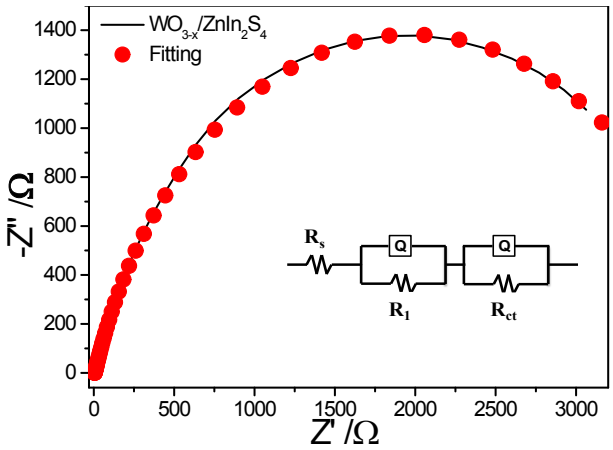

Supplementary Fig.9 The experimental and fitted EIS curves of the as-constructed $WO_{3-x}/ZnIn_2S_4$ catalyst. The inset is the equivalent circuit.

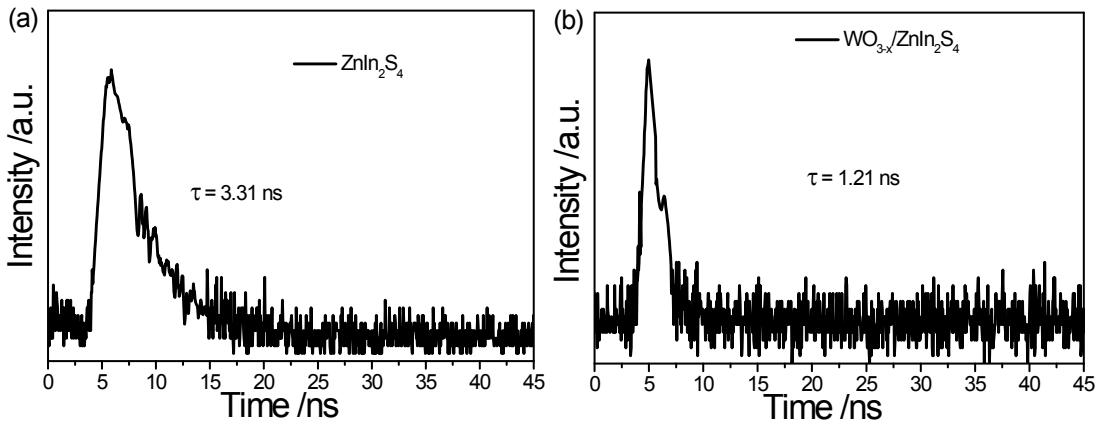

Supplementary Fig.10 The TRPL decay curves of $ZnIn_2S_4$ (a) and $WO_{3-x}/ZnIn_2S_4$ (b).

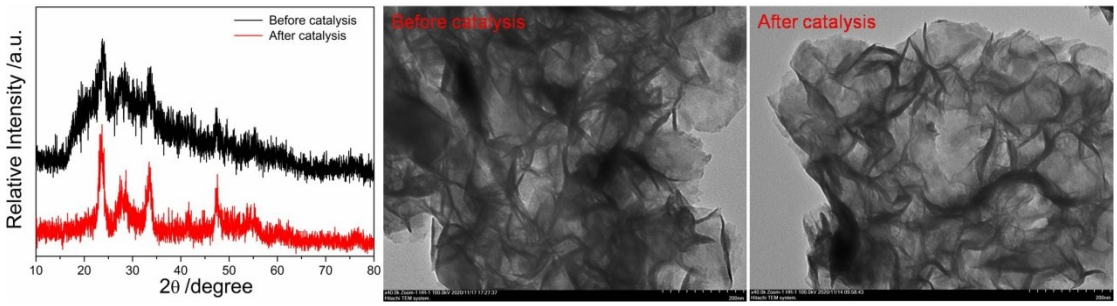

Supplementary Fig.11 XRD patterns and TEM images of the $WO_{3-x}/ZnIn_2S_4$ photocatalyst before and after durability tests.

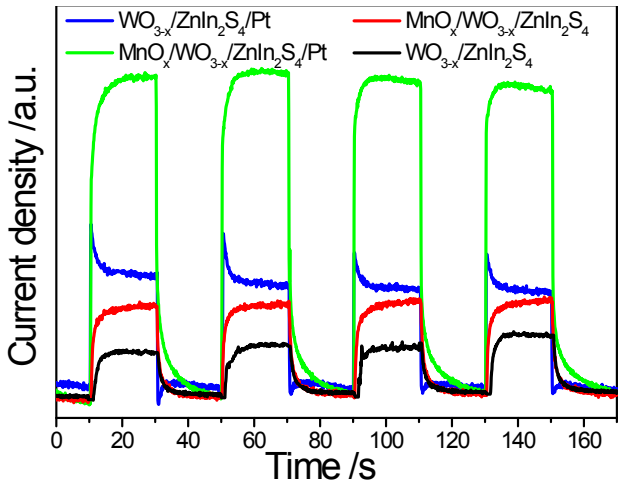

Supplementary Fig.12 the photocurrent responses of various catalysts.

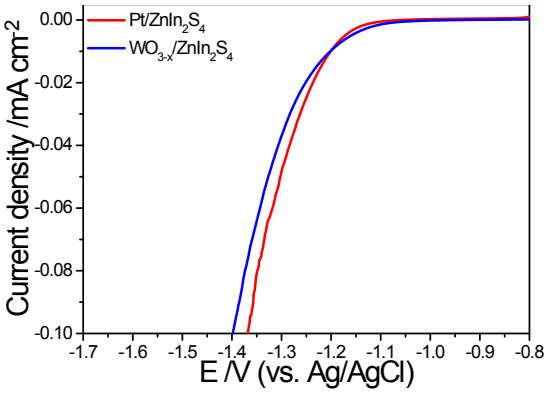

Supplementary Fig.13 the LSV curves of as-prepared $WO_{3-x}/ZnIn_2S_4$ and $Pt/ZnIn_2S_4$ catalysts.

Table S1. Atomic percentages of In, W, S and Zn elements in $WO_{3-x}/ZnIn_2S_4$ based on X-ray photoelectron spectroscopy.

Element	Atomic percentage /%
C	40.39
In	12.06
W	1.31
S	22.23
Zn	5.41
O	18.6

Table S2 Comparison of photocatalytic H_2 production performances of $WO_{3-x}/ZnIn_2S_4$ with some $ZnIn_2S_4$-based photocatalysts reported in the literatures.

Catalyst	Reaction Condition	H_2 generation rate ($\mu mol\ h^{-1}\ g^{-1}$)	Light Source	Refs.
$WO_{3-x}/ZnIn_2S_4$	TEOA	20957	AM1.5	This work
$WO_{3-x}/ZnIn_2S_4$	TEOA	5769	$\lambda > 400$ nm	This work
$ZnIn_2S_4@SiO_2@TiO_2$	TEOA	618	AM1.5	Inorg. Chem. 2020, 59, 2278-2287.
Ni_x-$ZnIn_2S_4$	TEOA	4220	$\lambda > 420$ nm	J. Mater. Chem. A 2020, 8, 13376.
$ZnIn_2S_4$/g-C_3N_4	TEOA	2640	$\lambda > 420$ nm	Appl. Catal. B 2018, 220, 542-552
$Co_9S_8@ZnIn_2S_4$	TEOA	6250	$\lambda > 400$ nm	J. Am. Chem. Soc. 2018, 140, 15145-15148.
Ultrathin $ZnIn_2S_4$ NSs with (110) facet exposure	TEOA	1940	$\lambda > 420$ nm	Appl. Catal. B. 2020, 265, 118616.
$ZnIn_2S_4$@CNO	TEOA,3wt% Pt	3760	$\lambda > 400$ nm	Chin. J. Catal. 2020, 41, 454-463.
O-doped $ZnIn_2S_4$	0.35 M Na_2S and 0.25 M Na_2SO_3	2120	$\lambda > 420$ nm	Angew. Chem. Int. Ed. 2016, 55, 6716-6720.
$ZnIn_2S_4$/1%$MoSe_2$	lactic acid	6454	$\lambda > 400$ nm	Nat. Commun. 2017, 8, 14224.
5%-$MoS_2/ZnIn_2S_4$	0.35 M Na_2S and 0.25 M Na_2SO_3	3891	$\lambda > 420$ nm	Appl. Catal. B 2018, 233, 112-119.
3wt%MoS_2/CQDs/$ZnIn_2S_4$	0.1M Na_2S/Na_2SO_3	3000	$\lambda > 420$ nm	J. Mater. Chem. A 2018, 6, 19735-19742.

Table S3 Comparison of photocatalytic H_2 evolution performances of $WO_{3-x}/ZnIn_2S_4$ with some non-$ZnIn_2S_4$-based photocatalysts

Catalysts	Reaction Conditions	Hydrogen generation rate (μmol h^{-1} g^{-1})	Light Source	Refs.
$WO_{3-x}/ZnIn_2S_4$	TEOA	20957	AM1.5	This work
$WO_{3-x}/ZnIn_2S_4$	TEOA	5769	λ > 400 nm	This work
CdS/Co_9S_8	0.35 M Na_2S and 0.25 M Na_2SO_3	1061	AM1.5	Angew. Chem. Int. Ed. 2017, 56, 2684 –2688.
γ-MnS/Cu_7S_4	0.35 M Na_2S and 0.25 M Na_2SO_3	700	AM1.5	Angew. Chem. Int. Ed. 2017, 56, 4206 –4210.
Ti^{3+} self-doped TiO_2	CH_3OH	181	λ > 400 nm	Angew. Chem. Int. Ed. 2012 124, 6223.
20%-MIL-125-$(SCH_3)_2$	TEOA	3814	λ > 400 nm	Angew. Chem. Int. Ed. 2018, 57, 9864-9869
$MoSe_2$/g-C_3N_4	TEOA	137	λ > 420 nm	Appl. Catal. B 2018, 233, 26-34.
BP/CN	CH_3OH	43	λ > 420 nm	J. Am. Chem. Soc. 2017, 139, 13234-13242.
Few-layer C_3N_4	TEOA, 1wt% Pt	7990	λ > 420 nm	J. Am. Chem. Soc. 2019, 141, 2508−2515
HM-TiPPh	TEOA, Pt co-catalyst	945	λ > 420 nm	Angew. Chem. Int. Ed. 2018, 57, 3222-3227.
CCTs	CH_3OH，3 wt% Pt	3538	λ > 400 nm	Angew. Chem. Int. Ed. 2018, 57, 1-8
1%Pt-Ti^{3+} self-doped TiO_2	CH_3OH	50	λ > 400 nm	J. Am. Chem. Soc., 2010, 132, 11856.
HNMT-Ir/Pt	TEOA	201	λ > 400 nm	Angew. Chem. Int. Ed. 2018, 57, 3493-3498
Al-TCPP-0.1Pt	TEOA	129	λ > 380 nm	Adv. Mater. 2018, 30, 1705112
Pt@UiO-66-NH_2	TEOA	257	λ > 380 nm	Angew. Chem. Int. Ed. 2016, 55, 9389-9393
1%PtO/TiO_2	CH_3OH	4400	Xe lamp, 300 W	Nat. Commun. 2015, 6, 5881.
0.16%Pt/g-C_3N_4	TEOA	6360	Xe lamp, 300 W	Adv. Mater. 2016, 28, 2427.
TiO_2/C_3N_4	TEOA，1wt% Pt	770	AM1.5	Appl. Catal. B 2016, 191,

				130-137
Defective meso-TiO_2	CH_3OH, 1wt% Pt	19800	AM1.5	Angew. Chem. Int. Ed. 2020, 59, 2-10.
0.6%Pt/TiO_2	CH_3OH	10000	AM1.5	Science. 2011, 331, 746.
1%Pt-Sub-10nm rutile TiO_2 nanoparticles	CH_3OH	1954	AM1.5	Nat. Commun. 2015, 6, 5881.
0.5% Pt-S doped H-TiO_2	CH_3OH	258	AM1.5	J. Am. Chem. Soc. 2013, 135, 17831.

Table S4 The solution resistance (R_s), charge transport resistance within the electrode (R_{ct}) and charge transfer resistance at the solid/electrolyte interface (R_1) of the $WO_{3-x}/ZnIn_2S_4$/NF electrode.

R/Ω	R_s	R_1	R_{ct}
$WO_{3-x}/ZnIn_2S_4$	5.33	22.77	3863